Computers & Fluids 114 (2015) 110–120

Contents lists available at ScienceDirect

Computers & Fluids

journal homepage: www.elsevier.com/locate/compfluid

Numerical study on dynamic sorting of a compliant capsule with a thin shell

Huilin Ye, Haibo Huang *, Xi-yun Lu

Dept. of Modern Mechanics, Univ. of Sci. and Tech. of China, Hefei 230026, China

ARTICLE INFO

Article history:
Received 4 December 2014
Received in revised form 10 February 2015
Accepted 28 February 2015
Available online 9 March 2015

Keywords:
LBM
LSM
Shear flow
Deformable particle
Narrow channel
Multi-particles

ABSTRACT

Sorting compliant capsules is an interesting research topic. In this paper, a simple bifurcated micro-channel is used to sort the particles with different rigidities. The behavior of a compliant particle inside the channel is investigated numerically. The fluid flow and the particle's deformation are solved by Lattice Boltzmann Method (LBM) and Lattice Spring Model (LSM), respectively. The fluid and solid solvers are coupled through interpolated bounce-back scheme. Two benchmark problems are used to validate our method. One is the motion of a compliant capsule in a channel and the other is the deformation of a capsule inside a simple shear flow. The results are quantitatively consistent with those in literature. By taking advantage of the rotating of capsules in shear flow, a simple distinguished bifurcated micro-channel is proposed to sort capsules with different rigidities. In this micro-channel, the initial offset and shear stress induce the rotating and lateral migration of the capsule and flux ratio is determined by the outlet pressures. The competition between the effect of initial offset and flux ratio contributes to the sorting mechanism. Compared to other micro-channels with different geometrical models, present one is more convenient and may be more efficient to screen the microcapsule we want.

1. Introduction

In recent years, researchers are very interested in the deformation and motion behavior of a capsule enclosed with elastic membrane. A possible reason is that behavior of a capsule immersed in fluid is similar to that of a Red Blood Cell (RBC) suspended in plasma. As we know, the RBC plays important role in Oxygen transfer. The RBC is enclosed with lipid bilayer, which would protect the entity of the cell and afford the ability to deform. The RBC suspended in blood on one hand is driven to flow with the blood, on the other hand is deforming under the effect of the fluid enclosing it. Hence, understanding the motion and deformation behavior of the RBC is important. In blood diseases like cerebral malaria and sickle cell anemia, the rigidity of RBC would be affected much [1]. When the RBC goes through the constricted capillary tube, it may be unable to deform enough and in a certain condition, it may be destroyed by a little stimulant such as some impurity contained in blood. For the application of capsules, artificial capsules are often used in the pharmaceutical, cosmetics, and food industries. They could regulate the release of active substances and flavors. Because of the small size and fragility, measuring the mechanical properties of the membrane is very difficult.

Research in membrane hydrodynamics has achieved great success. It leads to numerous membrane constitutive laws. The simplest law is Hooke's law restricted to small deformations. Another is Mooney–Rivlin (MR) law which assumed the membrane is a very thin sheet [2]. In order to model the large deformations of RBC, Skalak et al. [3] proposed the Skalak (SK) Law. Some theoretical studies have been carried out. Barthes-Biesel [4] and Barthes-Biesel and Rallison [5] applied a regular perturbation to analyze cases where the deviation from spherical shape of the capsule is small or large. Barthes-Biesel et al. [6] also compared the effect of constitutive laws for two dimensional (2D) membranes. They found that after a continuous elongation, a capsule with a MR membrane bursts, while a capsule with a SK membrane would reach a steady state.

However, deformation of a RBC depends on not only the elastic of the membrane, but also the flow of fluid surrounding the RBC. The flows in complex geometry are difficult to be analyzed theoretically. To study the deformation, usually experimental and numerical methods are adopted. To investigate the deformation of a capsule in a simple shear flow, Chang and Olbricht [7] and Walter et al. [8] designed artificial capsules composed of different material. However, usually it is difficult to change the rigidity of the capsule in experiments. With the development of numerical methods and computers, more researchers carried out relevant numerical studies [9–17].

* Corresponding author.

http://dx.doi.org/10.1016/j.compfluid.2015.02.021
0045-7930/

Many numerical methods have been developed to solve both the deformation of the capsule and fluid flow. For example, Woolfenden and Blyth [18] used boundary element method to solve both the solid and fluid parts. Immersed-boundary method (IBM) is another simple but effective scheme to solve the flow problem. The IBM is introduced by Peskin [19], and developed by Feng et al. [20], which is usually used to simulate the moving boundary problem. In the scheme, the deformation of capsule and fluid flow are solved separately and the IBM is used to couple the solutions. For example, MacMeccan et al. [21] and Sui et al. [11] applied the finite element analysis (FEA) and Lattice Boltzmann Method (LBM) to solve the dynamics of the membrane and fluid flow, respectively. The IBM is adopted to couple the FEA and LBM. This method is able to simulate large numbers of capsules suspended in fluid efficiently [12]. Sui et al. [9,10] identified various types of motion for a capsule freely suspended in simple shear flow. For an initially spherical capsule, it would exhibit a steady "tank-treading" motion, wherein the capsule deforms into a stationary shape with a finite inclination with the flow direction and the membrane would rotate around the interior liquid. Keller and Skalak [22] analyzed the motion of a viscous ellipsoid and investigated the effect of viscosity ratio of the inner and outer fluids. They found the critical viscosity ratio for a capsule translating from tank-treading motion to tumbling motion. Abkarian et al. [23] and Skotheim and Secomb [24] found that lowering the shear rate of the external flow could trigger the transition from successive swinging mode to the pure tumbling mode. Kessler et al. [25] concluded a full phase diagram for varying shear rate and viscosity ratio.

For studies of capsules sorting, Alexeev et al. [26–28] came up with an idea about capsules that are driven by a shear flow going through compliant substrates or corrugated surfaces. The motion of capsules can be controlled through changing rigidity of the substrates or corrugated structure. Zhu et al. [29] designed a constricted pillar geometrical model to regulate the motion of capsule because the velocity of the capsule depends on the rigidity of the capsule. However, the above sorting methods are not easily and efficiently applied in engineering. Now, more and more researchers try to design different mechanism to sort capsules with different rigidity.

Here, taking advantage of "tank treading motion", we designed a simple bifurcated micro-channel to sort capsules with different rigidities. Through setting different pressures on the outlet boundaries of the device, we can control which sub-channel the capsules will enter into. In the literature, there are some studies on capsules' behavior near the bifurcation. Woolfenden and Blyth [18] conducted a two-dimensional elastic fluid-filled capsule through a channel with a side branch. The deformation experienced by the capsule near the junction of main channel and side branch is found to depend strongly on the branch angle, and the path selection of a cell at a branch junction can depend crucially on the capsule deformability [18]. Hyakutake et al. [30] and Barber et al. [31] used 2D bifurcation flow to investigate the blood cell behavior at micro-vascular bifurcations. They found the fractional particle flux to a daughter branch is almost similar to the fractional bulk flow to the same branch in high hematocrit. However, in low hematocrit, the fractional particle flux against the fractional bulk flow increases. Hence, in previous relevant studies, no one focused on sorting capsules using simple bifurcated micro-channel.

To evaluate the performance of the device we designed, we take a numerical study on the sorting mechanism. Our numerical method is based on that of Alexeev et al. [26]. Capsule is modeled as a fluid-filled elastic shell. The Lattice Spring Model (LSM) is used to solve the deformation of the shell [32–35]. This model is able to simulate the solid material constructed by isotropic homogeneous elastic medium [32]. In the model, discrete solid nodes are connected with linear springs. For the fluid flow, the LBM is used, which is an efficient solver for Navier–Stokes equations [36–38]. The interpolated bounce-back scheme is used to couple the fluid flow and deformation of the capsules. However, Omori et al. [14] has used the numerical test of tension-strain relations and the isotropic tension-area dilation relations for large deformation to demonstrate that the cross mesh type we used in our paper exhibits a strain-hardening behavior and strain-softening behavior,respectively. So we set the capsule's deformation relatively low ($Ca < 0.2$) in order to model the biological cell membranes which is local area incompressibility more closely.

In this paper, first the numerical methods about LBM and LSM are introduced briefly. Then the numerical method is validated by two benchmark problems. One is the motion of a compliant capsule in a channel and the other is the deformation of a capsule inside a simple shear flow. Finally, sorting mechanism of capsules with different rigidity through the bifurcated channel is explored.

2. Method

2.1. Lattice Boltzmann method

In our study, the fluid flow is solved using LBM. In the LBM, the Bhatnagar–Gross–Krook (BGK) approximation for the collision term is adopted [36]. In the lattice BGK method, a distribution function $f_i(\mathbf{x},t)$ is introduced to implicitly represent all relevant properties of the fluid. This distribution function satisfies the following lattice Boltzmann equation [36]:

$$f_i(\mathbf{x}+\mathbf{e}_i\Delta t, t+\Delta t) = f_i(\mathbf{x},t) - \frac{1}{\tau}(f_i(\mathbf{x},t) - f_i^{eq}(\mathbf{x},t)), \quad (1)$$

where $f_i(\mathbf{x},t)$ is the density distribution function in the discrete velocity $\mathbf{e}_i$ direction. $f_i(\mathbf{x},t)$ is functions of position $\mathbf{x}$ and time t. τ is a non-dimensional relaxation time which is related to the kinematic viscosity by $\nu = c_s^2(\tau - 0.5)\Delta t$. Usually in the LBM code, Eq. (1) is decomposed into two steps. One is the streaming step:

$$f_i(\mathbf{x}+\mathbf{e}_i\Delta t, t+\Delta t) = f_i^+(\mathbf{x},t), \quad (2)$$

the other is the collision step:

$$f_i^+(\mathbf{x},t) = f_i(\mathbf{x},t) - \frac{1}{\tau}(f_i(\mathbf{x},t) - f_i^{eq}(\mathbf{x},t)). \quad (3)$$

The equilibrium distribution function $f_i^{eq}(\mathbf{x},t)$ can be calculated as [36]

$$f_i^{eq}(\mathbf{x},t) = w_i\rho\left[1 + \frac{\mathbf{e}_i\cdot\mathbf{u}}{c_s^2} + \frac{(\mathbf{e}_i\cdot\mathbf{u})^2}{2c_s^4} - \frac{(\mathbf{u})^2}{2c_s^2}\right]. \quad (4)$$

In Eqs. (1) and (4), for the two-dimensional nine-velocity (D2Q9) model, $\mathbf{e}_i$s are given by [36]

$$[\mathbf{e}_0,\mathbf{e}_1,\mathbf{e}_2,\mathbf{e}_3,\mathbf{e}_4,\mathbf{e}_5,\mathbf{e}_6,\mathbf{e}_7,\mathbf{e}_8] = c\cdot\begin{bmatrix} 0 & 1 & 0 & -1 & 0 & 1 & -1 & -1 & 1 \\ 0 & 0 & 1 & 0 & -1 & 1 & 1 & -1 & -1 \end{bmatrix}.$$

In Eq. (4) the weighting coefficients $w_i = 4/9$, ($i = 0$), $w_i = 1/9$, ($i = 1, 2, 3, 4$), $w_i = 1/36$, ($i = 5, 6, 7, 8$). The lattice sound speed in the LBM [36] is $c_s = \frac{c}{\sqrt{3}}$ for the D2Q9 model, where $c = \frac{\Delta x}{\Delta t}$ is the ratio of lattice spacing Δx and time step Δt. Here, we define 1 lattice unit (Δx) as 1 *lu*, 1 time step (Δt) as 1 *ts*, and 1 mass unit as 1 *mu*.

In Eq. (4), ρ is the density of the fluid, which can be obtained from the zeroth order moment of f_i [36],

$$\rho = \sum_i f_i, \quad (5)$$

and ρ_0 is used to denote the average density of the fluid. The fluid velocity can be calculated through the first order moment of f_i [36],

$$\mathbf{u} = \frac{1}{\rho}\sum_i f_i \mathbf{e}_i. \tag{6}$$

Macroscopically, the LBM recovers the Navier–Stokes equations.

2.2. Lattice spring model

The deformation of an elastic capsule is solved by the lattice spring model [26]. In the model, the regularly spaced mass point and nodes are connected by harmonic springs. The lattice spring nodes are described in a Lagrange coordinate. The position of the node i in the Euler coordinates (fixed in space) is $\mathbf{r}_i$, which may change with time. The elastic energy on node $\mathbf{r}_i$ is [26,33]

$$E(\mathbf{r}_i) = \frac{1}{2}\sum_j k_j\left(r_{ij} - r_{ij}^{eq}\right)^2, \tag{7}$$

where r_{ij} and k_j are the length and the spring constant of the spring connecting $\mathbf{r}_i$ and $\mathbf{r}_j$, respectively. r_{ij} and r_{ij}^{eq} are the distance between $\mathbf{r}_i$ and $\mathbf{r}_j$, and its equilibrium length, respectively. Hence the summation is over all the springs connected with node $\mathbf{r}_i$. This results in spring forces acting on node $\mathbf{r}_i$ [26]

$$\mathbf{F}_s(\mathbf{r}_i) = \sum_j k_j\left(\frac{r_{ij} - r_{ij}^{eq}}{r_{ij}}\right)\mathbf{r}_{ij}. \tag{8}$$

Fig. 1 shows that the elastic capsule (a thin shell) is modeled as a cylindrically symmetric lattice of springs, which has n concentric layers and each layer consists N nodes. Gap between two adjacent layers is $\Delta r = \Delta x_{LS}$, where Δx_{LS} is the lattice spacing in the LSM. Hence, the thickness of capsule $h_s = (n-1)\Delta r$ and the lattice spacing $\Delta r = \Delta x_{Ls} = 2\pi(R - h_s/2)/N$, where R is the radius of outermost layer.

As shown in Fig. 1, each lattice spring node is connected by orthogonal and diagonal springs. The spring constants for the orthogonal and diagonal springs are $2k$ and k, respectively [33]. For small deformations, this system of equations obey linear elasticity theory and results in a Young's modulus $E_s = 5k/2\Delta x_{LS}$ [33]. This simple model results in a Poisson's ratio $\nu_s = \frac{1}{4}$ [39,33]. This Poisson ratio is fixed in our study although more complicated many-body interactions can be included to change ν_s [33,41]. The sound speed in the solid is $c_s' = \Delta x_{LS}\sqrt{3k/M}$, and the solid density is $\rho_s = M/\Delta x_{LS}^2$, where M is the mass assigned to each lattice node.

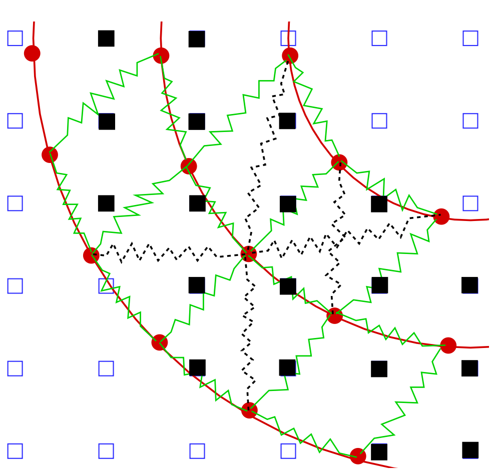

Fig. 1. Schematic diagram of lattice spring model. Open squares (□) and solid square (■) represent lattice Boltzmann nodes in fluid and solid, respectively. Solid circles (●) denote Lattice spring nodes. The solid and dotted springs represent orthogonal and diagonal connections, respectively.

After getting the force exerted by the fluid on the solid, we could integrate Newton's equation of motion,

$$\mathbf{F}(\mathbf{r}_i) = M(\partial^2\mathbf{r}_i/\partial t^2), \tag{9}$$

to capture the dynamics of solid. The following Verlet algorithm is used to integrate Eq. (9), which is a well-know method to update position $\mathbf{r}_i$, velocity $\mathbf{v}_i$, and acceleration $\mathbf{a}_i$ of each node at discrete time $t + \Delta t$ [32,33].

$$\begin{aligned}
&\mathbf{r}_i(t+\Delta t) = \mathbf{r}_i(t) + \mathbf{v}_i(t)\Delta t + \frac{1}{2}\mathbf{a}_i(t)\Delta t^2,\\
&\mathbf{v}_i\left(t+\frac{\Delta t}{2}\right) = \mathbf{v}_i(t) + \frac{1}{2}\mathbf{a}_i(t)\Delta t,\\
&\mathbf{a}_i(t+\Delta t) = \frac{\mathbf{F}_i(t)}{M},\\
&\mathbf{v}_i(t+\Delta t) = \mathbf{v}_i\left(t+\frac{\Delta t}{2}\right) + \frac{1}{2}\mathbf{a}_i(t+\Delta t)\Delta t.
\end{aligned} \tag{10}$$

This is a explicit scheme, so it requires that we should choose appropriate lattice spacing and time step to satisfy stability purpose. For our scheme, we only need to ensure that the Courant number $Cr = c_s'\Delta t_{LS}/\Delta x_{LS}$ is smaller than one. Further stability conditions are displayed in reference [28].

2.3. Solid–fluid coupling

For the solid–fluid coupling, as shown in Fig. 1, part of the fluid nodes would be overlapped by the lattice spring nodes (solid nodes). For these fluid nodes overlapped by solid nodes, the collision step is not implemented. There is no interaction between the overlapped fluid nodes and the lattice spring nodes. But the solid–fluid coupling does exist between the outmost (or innermost) lattice spring nodes and the fluid nodes next to them.

Here, the interaction between the outmost lattice spring nodes and its nearby fluid nodes is taken as a example. Usually, the outmost boundary of the capsule is supposed to be a curved wall. The coupling takes into account in this way: the fluid force acting on the curved wall boundary would be distributed to the nearby solid nodes (lattice spring nodes) on the curved wall by interpolation. Then according to Newton's equation of motion, position $\mathbf{r}_i$ and velocity $\mathbf{v}_i$ of each lattice spring node are updated (see Section 2.2). After $\mathbf{v}_i$ is known, the fluid solver (LBM) should take into account the movement of each small curved wall segment (outmost layer of the solid nodes). Through applying this 'new' moving boundary condition, the fluid field should be updated (see Section 2.1). Through this explicit iteration procedure, the solid and fluid solvers are well coupled [26,33].

In the follows, two key issues mentioned above will be introduced briefly. One is how to calculate the fluid force acting on the solid nodes on the outmost layer of the capsule, the other is how to take into account the moving wall effect in the LBM solver.

2.3.1. Fluid force acting on outmost lattice spring nodes

Fig. 2 shows the schematic diagram of fluid–solid coupling. We can see that near the curved wall, there are many intersections on the wall "b1", "b2", ... when connecting the fluid nodes and its neighboring overlapped nodes. Suppose the micro fluidic force act on these intersections, the force should be distributed to the lattice spring nodes (the large red disks on the curved wall in Fig. 2). In the follows, an example is used to explain this point.

The force on the intersections can be calculated through the momentum exchange scheme [37]. For example, the fluid force acting on node "b2" in the direction of $\mathbf{e}_\alpha = \mathbf{e}_5$ is (see Fig. 2).

$$\mathbf{F}^{(b)}\left(\mathbf{x}_{b2}, t+\frac{\Delta t}{2}\right) = \mathbf{e}_\alpha\left[f_\alpha^+(\mathbf{x}_f, t) + f_{\bar{\alpha}}(\mathbf{x}_f, t+\Delta t)\right], \tag{11}$$

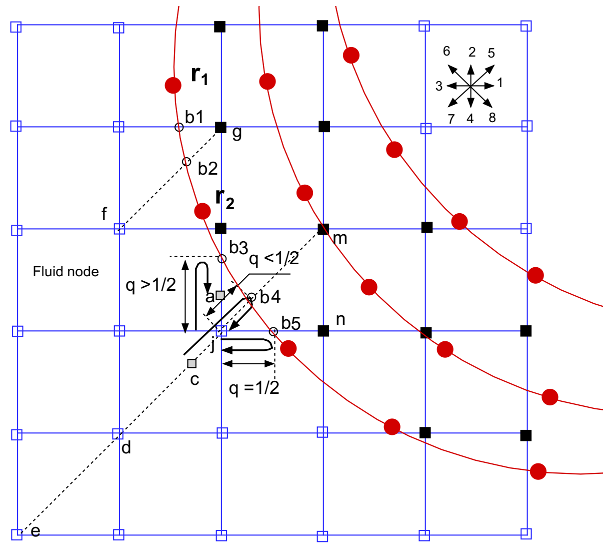

Fig. 2. Schematic diagram of fluid–solid coupling. Open squares (□) and solid square (■) represent lattice Boltzmann nodes in fluid and overlapped by capsule, respectively. The red disks are lattice spring nodes. Open circles (○) are intersections on curved wall when fluid nodes connecting its neighboring overlapped nodes. The gray solid squares are located in the fluid region but not on grid nodes. The thin blue solid lines are the grid lines. The thick arrows represent the trajectories of a 'particle' (a distribution function) interacting with the wall. (For interpretation of the references to colour in this figure legend, the reader is referred to the web version of this article.)

where $e_{\bar{\alpha}}$ means the reverse direction of e_α, i.e., $\mathbf{e}_{\bar{\alpha}} = -\mathbf{e}_\alpha$. $\mathbf{x}_f$ means the position of the node "f".

After the micro fluidic force acting on the wall node ($\mathbf{x}_{b2}$) is known, it can be distributed to the nearby lattice spring nodes ($\mathbf{r}_1$, and $\mathbf{r}_2$):

$$\mathbf{F}^{(b)}\left(\mathbf{r}_1, t+\frac{\Delta t}{2}\right) = (1-s)\mathbf{F}^{(b)}\left(\mathbf{x}_{b2}, t+\frac{\Delta t}{2}\right), \tag{12}$$

and

$$\mathbf{F}^{(b)}\left(\mathbf{r}_2, t+\frac{\Delta t}{2}\right) = s\mathbf{F}^{(b)}\left(\mathbf{x}_{b2}, t+\frac{\Delta t}{2}\right), \tag{13}$$

where $s = \frac{|\mathbf{x}_{b2}-\mathbf{r}_1|}{|\mathbf{r}_2-\mathbf{r}_1|}$. The other micro forces acting on the membrane can also be distributed in a similar way.

2.3.2. Moving curved wall boundary condition

On the other hand, the effect of movement of the curved wall should be involved in the LBM solver. Physically, the fluid flow at wall should satisfy the no-slip boundary condition. To handle curved wall boundary in the LBM, the most simple and successful treatment was proposed by Bouzidi et al. [38]. Because the collision step is not applicable to the fluid nodes occupied by capsule, for the fluid node which is nearest the wall, the distribution functions in some direction are actually unknown after streaming step. For example, in Fig. 2, for the fluid node "j", distribution functions f_3, f_4, f_7 are unknown.

To include the effect of curved wall in the LBM solver, the unknown distribution functions should be reconstructed. The main idea of Bouzidi et al. [38] is using Lagrange interpolation to obtain unknown distribution functions and extrapolation is avoided to improve numerical stability. Lallemand and Luo [37] later developed it taking account of the moving wall. It is introduced briefly in the follows.

In Fig. 2, the fluid and solid regimes are separated by the wall (solid red curved line). The D2Q9 velocity model is illustrated in the upper right corner. In the figure, q is defined as the fraction of the intersection link in the fluid region, e.g., for node $\mathbf{x}_j$ in $\mathbf{e}_5$ direction,

$$q = \frac{|\mathbf{x}_j - \mathbf{x}_{b4}|}{|\mathbf{x}_j - \mathbf{x}_m|}, \tag{14}$$

and for node $\mathbf{x}_j$ in $\mathbf{e}_1$ direction $q = \frac{1}{2}$.

The simplest reconstruction case is the case $q = \frac{1}{2}$. The actual position of the wall is located at "b_5", which is one-half grid spacing beyond the fluid node "j". The unknown $f_3(\mathbf{x}_j, t+\Delta t)$ is reconstructed by [38] $f_3(\mathbf{x}_j, t+\Delta t) = f_1^+(\mathbf{x}_j, t)$. It looks like the particle in $\mathbf{e}_1$ direction at node "j" bounces back after it collides with the wall (see Fig. 2).

Another example about the reconstruction of unknowns is case $q < \frac{1}{2}$. At time t, the distribution function $f_5^+(\mathbf{x}_c, t)$ at the point "c", which located at a distance $\sqrt{2}(1-2q)\Delta x$ away from the grid point "j" would end up at the grid point "j" after bounce back collision. That is indicated by a thick bent arrow in Fig. 2. Because $f_7(\mathbf{x}_j, t+\Delta t) = f_5^+(\mathbf{x}_c, t)$, the unknown $f_5^+(\mathbf{x}_c, t)$ can be reconstructed by a quadratic interpolation [38]:

$$f_5^+(\mathbf{x}_c, t) = q(1+2q)f_5^+(\mathbf{x}_j, t) + (1-4q^2)f_5^+(\mathbf{x}_d, t) - q(1-2q)f_5^+(\mathbf{x}_e, t). \tag{15}$$

Study of Lallemand and Luo [37] provides more general formulas for moving boundary. Suppose the wall boundary moves with velocity $\mathbf{u}_w$, to account for this moving effect, an extra term should be added into the above equations. In practice, it is more convenient to combine collision and streaming step together. Hence, more general formulas for unknown "$f_{\bar{\alpha}}(\mathbf{x}_j, t)$" taking the effect of moving boundary can be written as the follows. For the case of $q < \frac{1}{2}$,

$$\begin{aligned} f_{\bar{\alpha}}(\mathbf{x}_j, t) &= q(1+2q)f_\alpha(\mathbf{x}_j + \mathbf{e}_\alpha \Delta t, t) + (1-4q^2)f_\alpha(\mathbf{x}_j, t) \\ &\quad - q(1-2q)f_\alpha(\mathbf{x}_j - \mathbf{e}_\alpha \Delta t, t) + w_{\bar{\alpha}}\rho\frac{(\mathbf{e}_{\bar{\alpha}} \cdot \mathbf{u}_w)}{c_s^2}. \end{aligned} \tag{16}$$

For more details about the curved wall boundary condition, please refer to Ref. [37].

It is note that the moving velocity on the intersections can be constructed by interpolation from the velocities on nearby lattice spring nodes:

$$\mathbf{u}_{b2} = (1-s)\mathbf{u}(\mathbf{r}_1, t) + s\mathbf{u}(\mathbf{r}_2, t). \tag{17}$$

The initial value of $\mathbf{u}(\mathbf{r}_1, t)$ and $\mathbf{u}(\mathbf{r}_2, t)$ are set to be zero (refer to Fig. 2). Through the above explicit strategy, the fluid flow and the translation and deformation of the capsule can be coupled effectively.

3. Validation

3.1. Validation I: Deformable capsule moving in a channel flow

The first benchmark flow problem is the steady motion of a compliant capsule moving in a 2D rigid channel [29]. It should be noticed that present numerical method is identical to that of Zhu et al. [29]. Fig. 3 shows the schematic diagram of this flow problem. Initially the capsule is circular and placed midway between the channel walls. In our simulations, the channel height and length are $H = 54\,lu$ and $L = 8H$, respectively. The channel's upper and lower walls are assumed to be rigid. Three cases with $D = 0.5H, 0.8H$, and $0.9H$ are simulated, where D is the capsule's initial diameter. The flow is driven by a fixed pressure drop between inlet and outlet boundaries $\Delta p = 1.44 \times 10^{-3} mu/(lu\,ts^2)$.

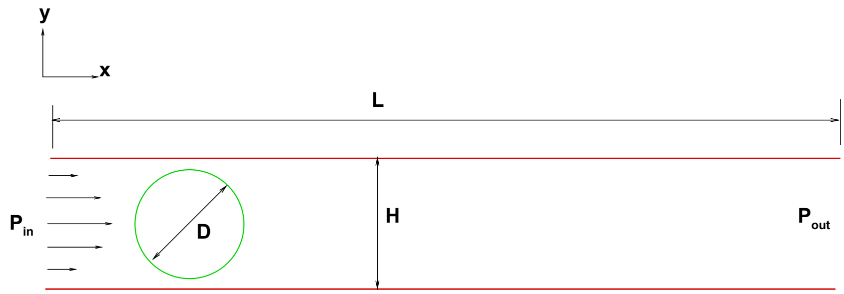

Fig. 3. Schematic diagram of a deformable capsule moving in a channel flow.

The pressure boundary condition proposed by Zou and He [42] is used. The shell consists three layers ($n = 3$) and lattice spring nodes per layer are approximately two times as many as the nodes used to discretize the diameter of the capsules. For example, the diameter of the capsule is $40\,lu$, i.e., the diameter is discretized into $40\ \Delta x$. Then the perimeter of the capsule is approximately $125.6\,lu$. Instead of 125 nodes, approximately 80 nodes are used to discretize the perimeter. Hence $\Delta x_{LS} \approx 1.57\,lu$.

In this flow, the Reynolds number is defined as

$$Re = \frac{U_0 D}{v}, \tag{18}$$

where v is the kinematic viscosity of the fluid and U_0 is the characteristic velocity. Here U_0 is chosen to be the mean velocity of the fluid within the channel without capsule driven by pressure drop Δp.

In this flow, Re is small and the inertia effect is negligible. Another important non-dimensional parameter in this flow is the Capillary number:

$$Ca = \mu \frac{U_0}{E_s h_c}, \tag{19}$$

where h_c denotes the thickness of capsule and $\mu = \rho v$ is the dynamic viscosity of the fluid. Ca is the ratio of viscous effect of fluid to elastic effect of capsule.

In Ref. [29], the final equilibrium moving velocities of the capsule are plotted. It is noted that the equilibrium shape of the capsule due to deformation is not given in Ref. [29]. However, if the equilibrium moving velocity agrees well with the data of Zhu et al. [29], the equilibrium deformation is expected to be very consistent with theirs since the equilibrium velocity highly depends on deformation.

In Fig. 4, the non-dimensional equilibrium velocity of the capsule V_r as a function of Ca is shown. Here V_r is defined as

$$V_r = \frac{V - U_0}{U_{max} - U_0}, \tag{20}$$

where V is the mass-averaged velocity of the capsule, and U_{max} is the maximal velocity of the fluid within the channel without capsule. For the Poiseuille flow in 2D channel without capsule, $U_{max} = 1.5U_0$.

It is seen that the velocity quantitatively agrees well with the data of Zhu et al. [29] for $D = 0.5H, 0.8H$ and $0.9H$. When $D = 0.5H, Ca$ effect on V_r is minor. For cases $D = 0.8H$ and $0.9H, V_r$ approximately increases linearly with Ca in the log–log coordinates. Hence, V_r and Ca approximately obey a power law. Hence, in this benchmark problem, our model does reproduce good results.

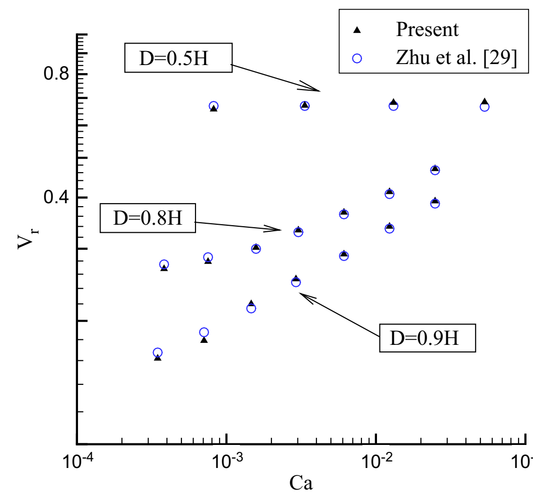

Fig. 4. The non-dimensional equilibrium velocity of the capsule V_r as a function of Ca for $D = 0.5H, 0.8H$, and $0.9H$ in log–log coordinates.

3.2. Validation II: Deformation of capsule in shear flow

The second benchmark flow problem is about an initial circular capsule freely suspended in a simple shear flow. The shear rate of the shear flow is γ, and the exterior and interior liquids are identical incompressible Newtonian fluids. In this flow, the definition of Ca and Re are identical to Eqs. (19) and (18) except for the characteristic velocity

$$U_0 = \frac{\gamma D}{2}, \tag{21}$$

where D is the diameter of the capsule. In this validation, the order of Re is about 10^{-2} and the inertia effect is negligible.

As showed in Fig. 5, the capsule is placed in the center of the computational domain, which is $L \times H = 20D \times 20D$ and $D = 40\,lu$. Periodic boundary conditions are applied in the flow direction (x-direction). The shell consists three layers and 80 lattice spring nodes per layer, i.e., $n = 3$, and $N = 80$. The corresponding $\Delta x_{LS} \approx \Delta r = 2\pi(D/2 - h_s/2)/N = 1.57\,lu$.

In follow simulations, we fixed γ and different Ca is achieved through adjusting the spring constant k. It is noted $E_s = \frac{5k}{2\Delta x_{LS}}$ is a monotonic function of k when Δx_{LS} is fixed.

Due to shear stress, the circular capsule shell would deform in the flow and finally reach an equilibrium state. Here the Taylor shape parameter D_{xy} is used to evaluate the deformation of the capsule, which is read

$$D_{xy} = \frac{L - B}{L + B}, \tag{22}$$

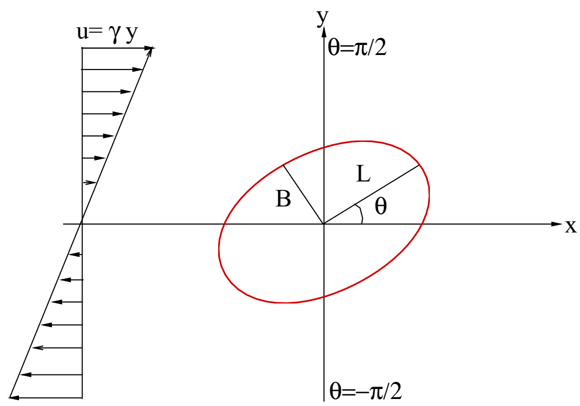

Fig. 5. Schematic of a capsule suspended in a shear flow.

where L and B are the lengths of the semi-major and minor axes of the equilibrium elliptical capsule, respectively (see Fig. 5). θ is the inclined angle (the major axis with respect to the horizontal x-axis).

Fig. 6 shows the deformation of capsules D_{xy} and the inclination angle θ as functions of time for cases with different Ca. It is seen that at beginning, deformation of the capsule D_{xy} in each case increases with time and finally reaches an equilibrium state. The equilibrium deformation of the capsule is large in the case with large Ca.

In each case, the inclination angle θ decreases with time at beginning and finally reach an equilibrium value. From Fig. 6(a) and (b), it is also observed that the time to reach equilibrium state also increases with Ca. In this benchmark problem, our results are quantitatively consistent with those of Breyiannis and Pozrikidis [44], which is obtained by boundary element method.

Here the grid-independence and time-step independence studies are also carried out. The case of $Ca = 0.0125$ and $Re = 10^{-2}$ is taken as an example. Cases with mesh size $\Delta x^* = \frac{\Delta x}{D} = 0.05, 0.02$, and 0.01 are simulated. The evolutions of D_{xy} are shown in Fig. 7(a). It is seen that $\Delta x^* = 0.05$ is fine enough to get accurate result for the case of $Ca = 0.0125$. For the time-step independence study, three cases with $\Delta t^* = \gamma \Delta t = 10^{-4}, 2 \times 10^{-4}, 8 \times 10^{-4}$ are simulated. The results is shown in Fig. 7(b). It is seen that time-step $\Delta t^* = 2 \times 10^{-4}$ is small enough to get accurate result. In the following simulations, $\Delta x^* = 0.05$ and $\Delta t^* = 2 \times 10^{-4}$ are adopted.

As we know, the relations for the material properties of LSM are derived for a linear elastic material, which is consistent with the Hooke's law [14,40]. Hence, it is expected that present LSM result will be consistent with that from the SK law when Ca is not large, because in the limit of small deformation, all laws including MR and SK laws are reduced to the 2D Hooke's law [14]. The comparison between present results and those of the SK-law membrane model [6,3] for $Ca < 0.2$ is shown in Fig. 8. In the figure, the results from the SK-law with $C = 0, 1$, and 10 are shown, where C is a parameter in the law and connected with Poisson's ratio by $\nu_s = \frac{C}{(1+C)}$ [6].

From Fig. 8, we can see that the results of the SK law [6] with $C = 0, C = 1$ almost collapse into a single curve while the curve of $C = 10$ is slightly lower than those of smaller C when $Ca > 0.05$. The results of the SK law [6] are independent of C for sufficiently small Ca. Present result is close to those of the SK law at $Ca < 0.2$. Due to the limitation of the LSM [14], to get reliable numerical result, the Ca in all of our simulation is limited to $Ca < 0.2$. The shape of the capsule in the case of $Ca = 0.2$ is also shown in Fig. 8.

The "tank treading motion" of membrane also occurs when a capsule reaches the equilibrium state in shear flow, i.e., the shell (Lagrange points) would rotate around the deformed profile. Fig. 9 shows the angular velocity of a Lagrange point as a function of time. After the initial transient, which depends on the initial flow field, dies out in the first period, the angular velocity becomes a perfect periodic function. It is noted that at the equilibrium state, the angular velocity at a Euler point occupied by the shell or the membrane is a constant.

Fig. 10 shows that the average angular velocity $\bar{\omega}$ of the shell as a function of Ca. $\bar{\omega}$ decreases with Ca and may asymptotically reaches a constant value. Hence, the "tank treading motion" becomes weak when Ca increases.

4. Motion in bifurcated channel

The characteristic "tank treading motion" discussed before has its own feature: the rotating direction of the shell would be consistent with the shear flow. This is one of the bases for sorting in our device. We would demonstrate that how the micro-channel is able to sort capsules.

The simple bifurcated channel designed by us is shown in Fig. 11. The widths of inlet and outlet of the domain are $H = H_1 = H_2 = 60\,lu$. The length of domain is $L = 300\,lu$. The capsule is initially placed at $L_1 = 50\,lu$ from the inlet. The other geometry parameters are $L_2 = 60\,lu, L_3 = 60\,lu$, and $L_4 = 80\,lu$. For the sub-channels, the inclined angle $\theta_0 = 35°$. An arc with $R_0 = 17\,lu$ is used to connect the two sub-channels. Radius of capsule is $R = 20\,lu$ and its thickness is $h_s = 3\,lu$. Pressures on the inlet of main channel and

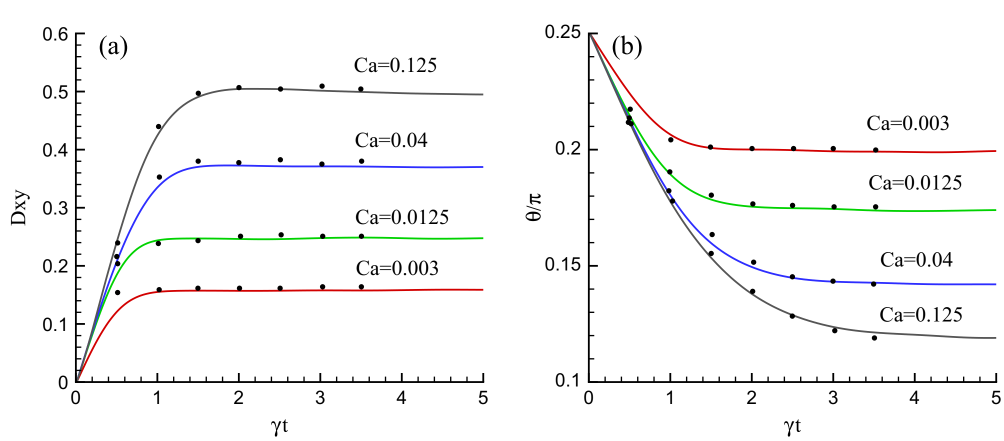

Fig. 6. Evolution of (a) Taylor shape parameter, (b) inclination angel for different Ca. Solid lines denote the present result, disks (•) denote the results of element method [44].

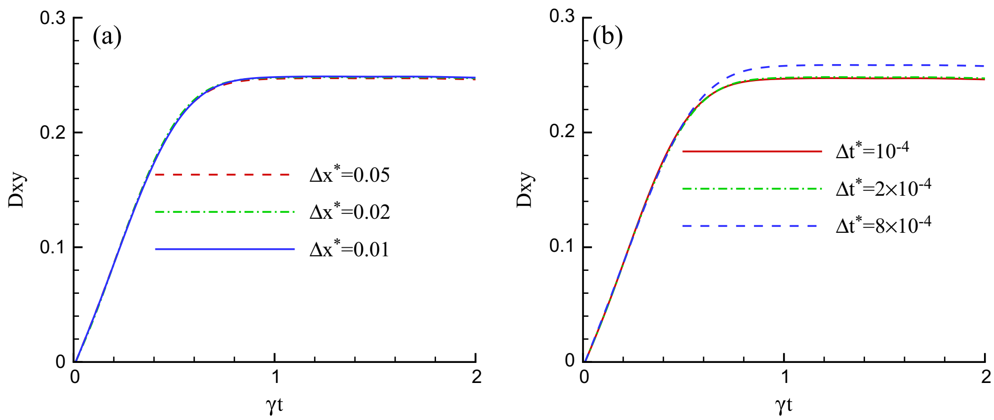

Fig. 7. Grid-independence study (a) and time-step independence study (b) for the case $Ca = 0.0125$ and $Re = 10^{-2}$.

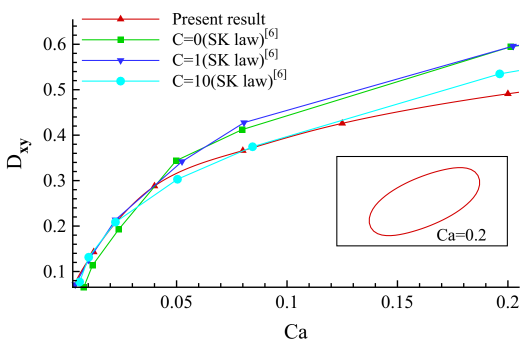

Fig. 8. D_{xy} as a function of Capillary number Ca. Present result is compared with that of SK law membrane [6].

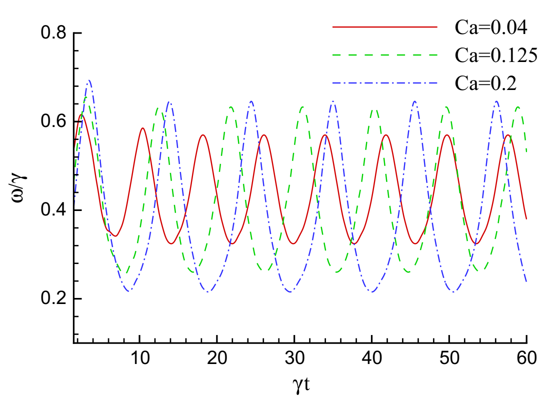

Fig. 9. Evolution of angular velocity of a material point (a lattice spring node) on the capsule with different Ca.

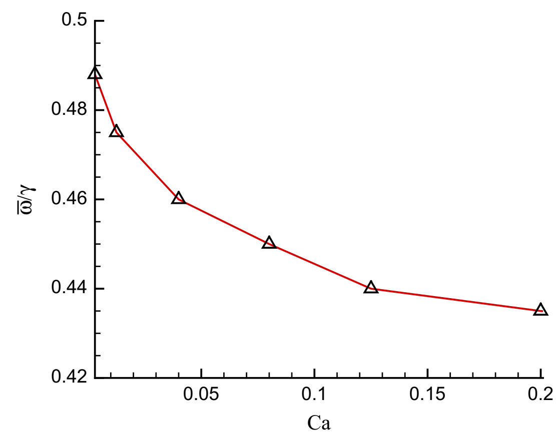

Fig. 10. Average angular velocity of shell as a function of Ca.

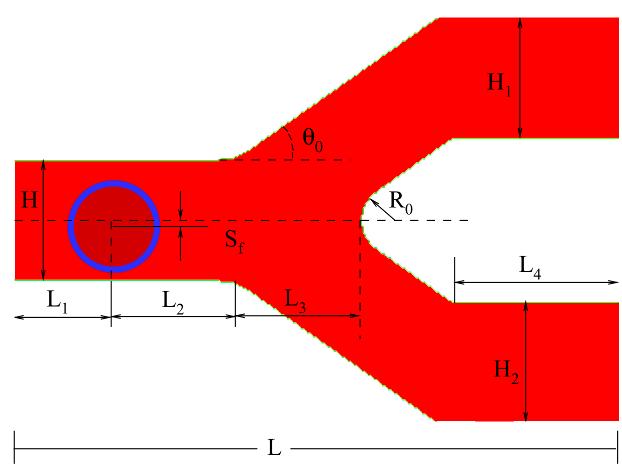

Fig. 11. Schematic diagram of bifurcated channel.

outlets of sub-channels are specified [42]. The capsule that immersed in flow domain moves with the flow and deforms under the effect of viscous force. The lattice spring nodes on the shell of the capsule are identical as that in Section 3.2, i.e., $n = 3$, and $N = 80$. The initial condition is that both the flow and capsule are stationary.

The Re and Ca are identical to those in Eqs. (18) and (19), respectively except the characteristic velocity

$$U_0 = \left(\frac{\Delta P}{L}\right)\frac{H^2}{12\mu}. \tag{23}$$

The Re is of $O(1)$, so the inertia effect is negligible.

If the circular capsule is initially placed in the center of the channel, i.e. $S_f = 0$, due to symmetry, the capsule will not rotate. Which sub-channel it will enter is only determined by the pressures in the outlets. For example, if the pressure on the upper outlet is lower, the capsule will enter the upper sub-channel. It has nothing to do with the rigidity of the capsule.

If initially there is a shift between the center of capsule and the central line of the channel, through changing the two outlet pressures, the motion of the capsule may be adjusted. In other words, the capsules with different rigidities may be sorted.

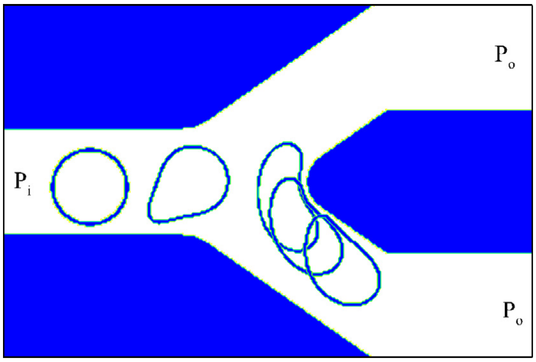

Fig. 12. Evolution of capsule moving in channel with $t^* = \frac{U_0 t}{H} = 0,\ 2,\ 6,\ 8,\ 10.$ and $S_f = 3\,lu$ and $Ca = 0.05$. The outlet pressures are $P_1' = P_2'$.

Firstly, the case with identical outlet pressures is considered. The inlet pressure is set to be $P_i = c_s^2\rho_0 + \frac{1}{2}L(\frac{\Delta P}{L})$, pressures in both upper and lower outlets are $P_o = c_s^2\rho_0 - \frac{1}{2}L(\frac{\Delta P}{L})$, where $\frac{\Delta P}{L} = 1.3\times10^{-6}\,mu/(lu^2ts^2)$. The capsule is initially placed below the symmetric line with an offset S_f, which is referred to as a negative offset. Otherwise, it is referred to as a positive offset. Due to symmetry of the channel, in the following discussion, only cases with a negative offset are discussed. Under the circumstances, Fig. 12 shows the motion of the capsule. We can see that the capsule would choose the lower sub-channel because of the initial negative offset when the pressures in both upper (P_1') and lower (P_2') outlets are identical, i.e., $P_1' = P_2' = P_o$. The time in this section is normalized by $\frac{H}{U_0}$.

Then we would like to discuss how the channel can be used to sort capsules with different rigidity. Taking the advantage of treading motion, the sorting may be controlled by the outlet pressures. For simplicity, the pressures in the upper (P_1') and lower outlets (P_2') are set to be

$$P_1' = c_s^2\rho_0 - \left(\frac{\Delta P}{L}\right)\frac{Q}{2}, \qquad P_2' = c_s^2\rho_0 + \left(\frac{\Delta P}{L}\right)\frac{Q}{2}, \tag{24}$$

respectively. It is noted that in the following study, $Q > 0$ and $P_1' < P_2'$. The inlet pressure P_i is fixed be $P_i = c_s^2\rho_0 + \frac{1}{2}L(\frac{\Delta P}{L})$. The pressures in the outlets are controlled by changing Q, which represents pressure difference between P_1' and P_2'. Suppose the Poiseuille flow is fully developed inside the channels without capsules, the flow rates inside upper and lower channels are $\widetilde{Q}_1$ and $\widetilde{Q}_2$, respectively. The flux ratio $\widetilde{Q}$ is defined as $\widetilde{Q} \equiv \frac{\widetilde{Q}_1}{\widetilde{Q}_2}$. Obviously, the flux ratio $\widetilde{Q}$ will increase with Q. Due to different flow fluxes entering the two branches, the capsule may be drawn to the branch with the higher flow rate [18,43].

In the following, cases with $Ca = 0.05$ are studied. Fig. 13(a) shows the motion of the capsule near the bifurcation. For the case $Q = 0.01$, the capsule still chooses the lower sub-channel. However, when $Q = 0.1$, Fig. 13(b) shows that the capsule enters the upper sub-channel, i.e., it moves to the sub-channel with lower pressure (P_1'). Hence, the pressure difference in outlets, i.e., the magnitude of Q would affect the movement of the capsule and determine which sub-channel the capsule will enter. In the follows, we would investigate the sorting effect due to Q systematically.

4.1. Ca–Q phase diagram

To find the critical Q for a specific Ca, we carried out many numerical simulations with different Q. For example, for cases with $Ca = 0.05$, ten simulations with $Q \in [0.01, 0.1]$ with an interval value of 0.01 were simulated. It is found the critical Q is approximate 0.05 for $S_f = 3\,lu$. Alternatively, we can fix Q and simulate cases with different Ca to find the critical Ca. Through a systematic numerical simulations, we find how the capsules can be controlled to enter the upper sub-channel with the initial negative offset.

Fig. 14 gives the phase-diagram about the movement of the capsules in the Ca–Q plane for different S_f. In Fig. 14(b), squares represent the normal movement of the capsule, i.e., entering lower sub-channel due to the negative offset. The trajectory is referred to as "normal path". In the lower left region of the Ca–Q plane, capsules adopt normal path, i.e., a very small Q has no effect on the normal choice of capsules. In contrast, triangles in the figure denote the capsule entering the upper sub-channel. The trajectory of this movement is referred to as "sorting path". From Fig. 14, we can see that for a specific Ca, above a critical Q, the capsule would follow the sorting path. Otherwise, the capsule would follow the normal path.

Obviously, to get more accurate phase-diagram requires much computational cost because the interval value of the simulations should be smaller. Here, we tried to find the border to separate the regimes of normal and sorting paths as accurate as possible. In Fig. 14(b), the border is represented by the solid line that connects the mid-values (circles) of the corresponding squares and triangles. Fig. 14(a) and (c) are obtained in the similar way. The phase-diagrams demonstrate the mechanism about using this channel to sort the capsules with different rigidities.

Here Fig. 14(b) with the initial negative offset $S_f = 3\,lu$ is taken as an example to illustrate how this equipment works in reality. Suppose we plan to sort capsules with $Ca \in (0.1, 0.15)$, we should use the equipment twice. In the first time, $Q \approx 0.02$ is adopted to get capsules with $Ca < 0.15$ in the lower sub-channel (capsules with $Ca > 0.15$ in the upper sub-channel). In the second time, let the capsules with $Ca < 0.15$ go through the equipment again with $Q \approx 0.03$, then from the upper sub-channel, we will obtain the capsules with $Ca \in (0.1, 0.15)$.

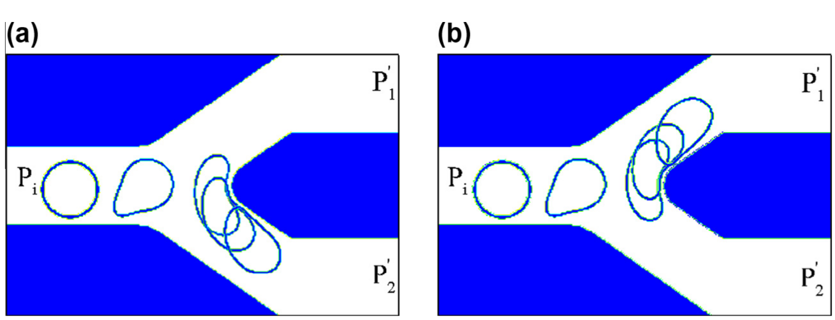

Fig. 13. Evolutions of a capsule moving in the channel for cases $S_f = 3\,lu, Ca = 0.05$ with $t^* = \frac{U_0 t}{H} = 0,\ 2,\ 6,\ 8,\ 10.$ (a) $Q = 0.01$, and (b) $Q = 0.1$.

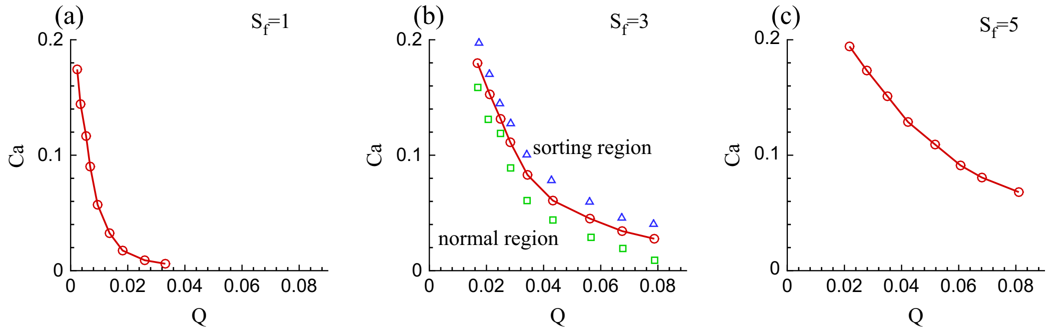

Fig. 14. *Ca–Q* phase-diagram about the movement of the capsules with different initial negative offset S_f. The triangles and squares denote capsules following "sorting path" and "normal path", respectively. (a) $S_f = 1\,lu$, (b) $S_f = 3\,lu$, (c) $S_f = 5\,lu$. The circles represent the mid-values of the corresponding squares and triangles.

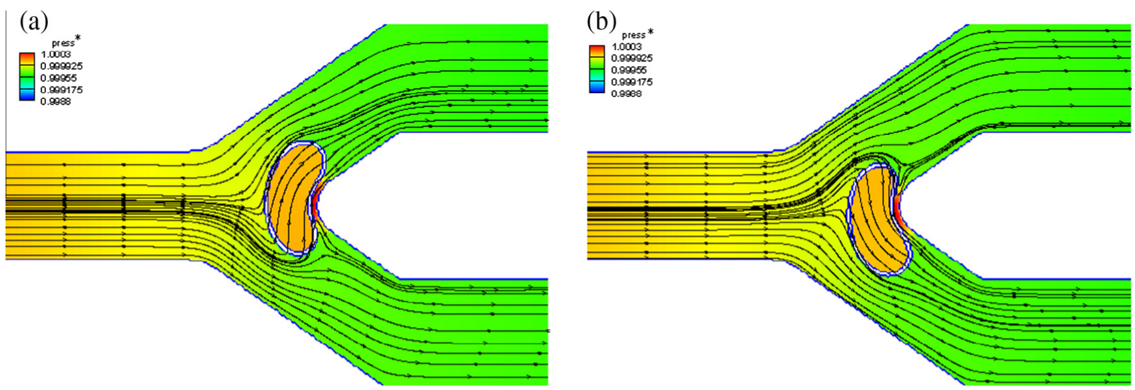

Fig. 15. Streamlines in flow fields (a) $Q = 0.1, Ca = 0.05$ and (b) $Q = 0.01, Ca = 0.05$. Pressure contours are normalized by the inlet pressure.

From Fig. 14(a), it is seen that for the initial offset $S_f = 1\,lu$, Ca decreases quickly with Q when Q is small. That means a small Q is required to sort capsules. However, in Fig. 14(a) the border is steep for $Ca \in (0.02, 0.15)$. Hence, to sort capsules with a specific $Ca \in (0.02, 0.15)$ when $S_f = 1\,lu$, pressure difference Q should be controlled more precisely. That may be a challenge in reality. We prefer the border lines like those in Fig. 14(b) and (c), which are not so steep.

4.2. Mechanism of sorting

When the capsule moves in the main channel, it would rotate clockwise and move upward due to the initial negative offset and shear stress in the Poiseuille flow. When it enter into the region near the joint, the rotating direction would change with different condition. Results of two cases are shown in Fig. 15. One case is $Q = 0.1, Ca = 0.05$, the other case is $Q = 0.01, Ca = 0.05$. They are referred to as Case A and Case B, respectively. In the two cases, the capsules adopt sorting path and normal path, respectively. Fig. 15(a) shows that in Case A, the capsule rotates clockwise, which keeps the original rotating direction. While in Case B (Fig. 15(b)), the capsule's rotation direction changes to counter-clockwise.

The capsule in shear flow will experience a lift force because the deformation of the capsule breaks the symmetry of the stokes flow when the capsule or vesicle near a wall [45]. In case of our scheme, Doddi and Bagchi [46] confirmed that the presence of the walls and parabolic nature of Poiseuille flow makes the capsule near the wall experience a deformation-induced lift force, which makes the capsule migrate to the center of the domain where the shear magnitude is low.

After the capsule translates to the region near the joint, the effect of flux ratio becomes dominant. If the flux ratio $\widetilde{Q}$ is large enough, the capsule would be drawn to the upper sub-channel. The capsule translates along the upper sub-channel and rotates clockwisely due to the shear stress in the upper sub-channel. On the contrary, if the flux ratio $\widetilde{Q}$ is small, the capsule would choose the lower sub-channel. The rotating direction would change because of the shear stress of Poiseuille flow in the lower sub-channel.

In summary, firstly, the capsule would translate along the main channel and migrate to the center of the channel due to the flow and the deformation-induced lift force [46]. Secondly, after the capsule leaves the main channel, due to the effect of the initial offset, the capsule would reach a specific place near the joint. At the place, if the flux ratio $\widetilde{Q}$ is large enough, the capsule would be drawn into the upper sub-channel and follow the sorting path. Otherwise, it would follow the normal path. In a whole, the initial offset and the flux ratio due to outlet pressures in sub-channels determine the behavior of the capsule.

4.3. Effect of viscosity ratio and initial distance

The viscosity ratio also plays an important role in the deformation of a capsule in flow [4,5], and in practical conditions, the internal fluid is always more viscous than the external one. In this section the effect of viscosity ratio on the sorting of capsule in the bifurcated channel is discussed.

Fig. 16 shows that for cases with $Ca = 0.05, Q = 0.05$ and lower viscosity ratio ($\lambda \leqslant 6$), the capsule would follow the sorting path. As λ increases ($\lambda > 6$, cases of $\lambda = 8$ and $\lambda = 10$), the capsule would follow the normal path (entering the lower sub-channel). When λ increases, a large flux ratio $\widetilde{Q}$ is required to force the capsule to follow the sorting path. That can be understood in the following way. When λ is large, the capsule looks like a solid body and the

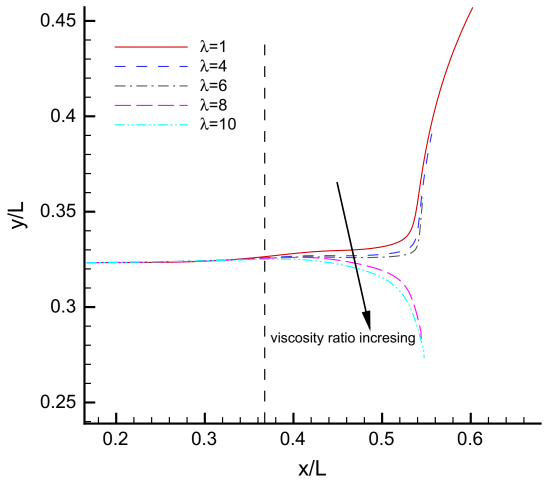

Fig. 16. The trajectory of the center of mass of the capsule with different viscosity ratio under the conditions of $Ca = 0.05, Q = 0.05$. The vertical dashed line represents the location of the outlet of the main channel.

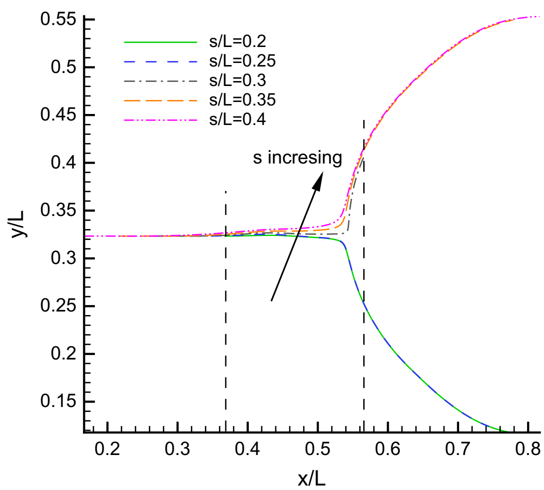

Fig. 17. The trajectory of the center of mass of the capsule with different initial distance of the capsule from the junction with the condition $Ca = 0.05, Q = 0.1$. s represents the initial distance. The left dashed line represents outlet of the main channel and the right represents the junction.

deformation of the capsule is smaller, which is similar to the cases with large rigidity.

From the discussion of mechanism, the rotation and lateral migration of the capsule is important. The distance between the capsule's initial place and the joint is referred to as the initial distance. If the initial distance is small, the lateral migration may be not close to the centerline of the main channel enough and the flux ratio may be unable to drawn the capsule into the upper sub-channel (sorting path).

Fig. 17 shows that when the initial distance is less than $0.25L$ with $Ca = 0.05, Q = 0.1$, the capsule would choose the normal path, this shows that a larger flux ratio (larger $\widetilde{Q}$) is required to guide it to the sorting path.

5. Conclusion

In this paper, behavior of a compliant capsule inside a bifurcated channel is studied through coupling the LBM and LSM. Two benchmark flow problems are used to validate our numerical method.

Although the results above are obtained through flows in a specific micro-channel, the mechanism of sorting capsules with different rigidities is demonstrated. Due to the initial offset of the capsule, it rotates in the main channel. Taking advantage of the rotating of capsules in shear flow (Poiseuille flow), the simple bifurcated micro-channel is able to sort capsules with different rigidities by adjusting the outlet pressures P'_1 and P'_2. Both initial offset, which induce the rotating and flux ratio due to P'_1 and P'_2 contribute to the sorting mechanism. Compared to other micro-channels with different geometrical model, present one is more convenient and may be more efficient to screen the microcapsule we want.

Two-dimensional simulations are able to qualitatively capture some behavior of real, three-dimensional capsules in a tube flow, such as the key features of the capsule profile and the lateral migration to the tube centerline [18]. On the other hand, we must confess that two-dimensional studies have some limitation when they describe the elastic behavior of the capsule membrane. For example, in-plane shear deformation occurs in three-dimensions but not in two-dimensions [18].

Hence, we plan to extend the present work to the three-dimensional setting to study the sorting behavior of a capsule in a bifurcated channel, where the capsule membrane mechanics conform to a physically realistic constitutive model, in the near future.

Acknowledgments

H. Huang is supported by National Natural Science Foundation of China (Grant No. 11172297), Program for New Century Excellent Talents in University, Ministry of Education, China (NCET-12-0506), and Anhui Provincial Natural Science Foundation (Grant No. 1308085MA06), China.

References

[1] Fung Y. Biomechanics: circulation. Springer; 1997.
[2] Mooney M. A theory of large elastic deformation. J Appl Phys 1940;11(9):582–92.
[3] Skalak R, Tozeren A, Zarda RP, et al. Strain energy function of red blood cell membranes. Biophys J 1973;13(3):245.
[4] Barthes-Biesel D. Motion of a spherical microcapsule freely suspended in a linear shear flow. J Fluid Mech 1980;100:831.
[5] Barthes-Biesel D, Rallison J. The time-dependent deformation of a capsule freely suspended in a linear shear flow. J Fluid Mech 1981;113:251.
[6] Barthes-Biesel D, Diaz A, Dhenin E. Effect of constitutive laws for two-dimensional membranes on flow-induced capsule deformation. J Fluid Mech 2002;460:211.
[7] Chang K, Olbricht W. Experimental studies of the deformation and breakup of a synthetic capsule in steady and unsteady simple shear flow. J Fluid Mech 1993;250:609.
[8] Walter A, Rehage H, Leonhard H. Shear induced deformation of microcapsules: shape oscillations and membrane folding. Colloids Surfaces A: Physicochem Eng Aspects 2001;183:123.
[9] Sui Y, Chew Y, Low H. A lattice Boltzmann study on the large deformation of red blood cells in shear flow. Int J Modern Phys C 2007;18:993.
[10] Sui Y, Chew Y, Roy P, Cheng Y, Low H. Dynamic motion of red blood cells in simple shear flow. Phys Fluids (1994-present) 2008;20:112106.
[11] Sui Y, Chew Y, Roy P, Low H. A hybrid method to study flow-induced deformation of three-dimensional capsules. J Comput Phys 2008;227:6351.
[12] Zhang J, Johnson PC, Popel AS. Red blood cell aggregation and dissociation in shear flows simulated by lattice Boltzmann method. J Biomech 2008;41:47.
[13] Xiong W, Zhang J. Two-dimensional lattice Boltzmann study of red blood cell motion through microvascular bifurcation: cell deformability and suspending viscosity effects. Biomech Model Mechanobiol 2012;11:575.
[14] Omori T, Ishikawa T, Barthès-Biesel D, Salsac A-V, Walter J, Imai Y, et al. Comparison between spring network models and continuum constitutive laws: application to the large deformation of a capsule in shear flow. Phys Rev E 2011;83:041918.
[15] Omori T, Imai Y, Yamaguchi T, Ishikawa T. Reorientation of a nonspherical capsule in creeping shear flow. Phys Rev Lett 2012;108:138102.
[16] Aidun CK, Clausen JR. Lattice-Boltzmann method for complex flows. Annu Rev Fluid Mech 2010;42:439.
[17] Clausen JR, Aidun CK. Capsule dynamics and rheology in shear flow: particle pressure and normal stress. Phys Fluids (1994-present) 2010;22:123302.

[18] Woolfenden H, Blyth M. Motion of a two-dimensional elastic capsule in a branching channel flow. J Fluid Mech 2011;669:3.
[19] Peskin CS. The immersed boundary method. Acta Numer 2002;11.
[20] Feng Z-G, Michaelides EE. Proteus: a direct forcing method in the simulations of particulate flows. J Comput Phys 2005;202:20.
[21] MacMeccan RM, Clausen J, Neitzel G, Aidun C. Simulating deformable particle suspensions using a coupled lattice-Boltzmann and finite-element method. J Fluid Mech 2009;618:13.
[22] Keller SR, Skalak R. Motion of a tank-treading ellipsoidal particle in a shear flow. J Fluid Mech 1982;120:27.
[23] Abkarian M, Faivre M, Viallat A. Swinging of red blood cells under shear flow. Phys Rev Lett 2007;98:188302.
[24] Skotheim J, Secomb T. Red blood cells and other nonspherical capsules in shear flow: oscillatory dynamics and the tank-treading-to-tumbling transition. Phys Rev Lett 2007;98:078301.
[25] Kessler S, Finken R, Seifert U. Swinging and tumbling of elastic capsules in shear flow. J Fluid Mech 2008;605:207.
[26] Alexeev A, Verberg R, Balazs AC. Designing compliant substrates to regulate the motion of vesicles. Phys Rev Lett 2006;96:148103.
[27] Alexeev A, Verberg R, Balazs AC. Motion of compliant capsules on corrugated surfaces: a means of sorting by mechanical properties. J Polym Sci Part B: Polym Phys 2006;44:2667.
[28] Alexeev A, Verberg R, Balazs AC. Modeling the motion of microcapsules on compliant polymeric surfaces. Macromolecules 2005;38:10244.
[29] Zhu G, Alexeev A, Kumacheva E, Balazs AC. Modeling the interactions between compliant microcapsules and pillars in microchannels. J Chem Phys 2007;127:034703.
[30] Hyakutake T, Matsumoto T, Yanase S. Lattice Boltzmann simulation of blood cell behavior at microvascular bifurcations. Math Comput Simul 2006;72:134.
[31] Barber JO, Alberding JP, Restrepo JM, Secomb TW. Simulated two-dimensional red blood cell motion, deformation, and partitioning in microvessel bifurcations. Ann Biomed Eng 2008;36:1690.
[32] Pazdniakou A, Adler P. Lattice spring models. Transport Porous Media 2012;93:243.
[33] Buxton G, Verberg R, Jasnow D, Balazs A. Newtonian fluid meets an elastic solid: coupling lattice Boltzmann and lattice-spring models. Phys Rev E 2005;71:056707.
[34] Buxton GA, Care CM, Cleaver DJ. A lattice spring model of heterogeneous materials with plasticity. Modell Simul Mater Sci Eng 2001;9(6):485.
[35] Ostoja-Starzewski M. Lattice models in micromechanics. Appl Mech Rev 2002;55:35.
[36] He X, Luo L-S. Theory of the lattice Boltzmann method: from the Boltzmann equation to the lattice Boltzmann equation. Phys Rev E 1997;56:6811.
[37] Lallemand P, Luo L-S. Lattice Boltzmann method for moving boundaries. J Comput Phys 2003;184:406.
[38] Bouzidi M, Firdaouss M, Lallemand P. Momentum transfer of a Boltzmann-lattice fluid with boundaries. Phys Fluids (1994-present) 2001;13:3452.
[39] Ladd AJ, Kinney JH. Elastic constants of cellular structures. Phys A: Stat Mech Appl 1997;240:349.
[40] Kilimnik A, Mao W, Alexeev A. Inertial migration of deformable capsules in channel flow. Phys Fluids (1994-present) 2011;23:123302.
[41] Schwartz LM, Feng S, Thorpe M, Sen PN. Behavior of depleted elastic networks: comparison of effective-medium and numerical calculations. Phys Rev B 1985;32:4607.
[42] Zou Q, He X. On pressure and velocity boundary conditions for the lattice Boltzmann BGK model. Phys Fluids (1994-present) 1997;9:1591.
[43] Fung YC. Stochastic flow in capillary blood vessels. Microvasc Res 1973;5(1):34C48.
[44] Breyiannis G, Pozrikidis C. Simple shear flow of suspensions of elastic capsules. Theor Comput Fluid Dynam 2000;13:327.
[45] Olla, Piero. The lift on a tank-treading ellipsoidal cell in a shear flow. J Phys II 1997;10:7.
[46] Doddi Sai K, Bagchi Prosenjit. Lateral migration of a capsule in a plane Poiseuille flow in a channel. Int J Multiphase Flow 2008;10:34.